

ApJ, in press August 2001 (Submitted March 2001)

Broad-band Observations and Modeling of the Shell-Type Supernova Remnant G347.3-0.5

Donald C. Ellison¹, Patrick Slane², and Bryan M. Gaensler^{3,4}

ABSTRACT

The supernova remnant G347.3–0.5 emits a featureless power-law in X-rays, thought to indicate shock-acceleration of electrons to high energies. We here produce a broad-band spectrum of the bright NW limb of this source by combining radio observations from the Australia Telescope Compact Array (ATCA), X-ray observations from the Advanced Satellite for Cosmology and Astrophysics (ASCA), and TeV γ -ray observations from the CANGAROO imaging Čerenkov telescope. We assume this emission is produced by an electron population generated by diffusive shock acceleration at the remnant forward shock. The nonlinear aspects of the particle acceleration force a connection between the widely different wavelength bands and between the electrons and the unseen ions, presumably accelerated simultaneously with the electrons. This allows us to infer the relativistic proton spectrum and estimate ambient parameters such as the supernova explosion energy, magnetic field, matter density in the emission region, and efficiency of the shock acceleration process. We find convincing evidence that the shock acceleration is efficient, placing $> 25\%$ of the shock kinetic energy flux into relativistic ions. Despite this high efficiency, the maximum electron and proton energies, while depending somewhat on assumptions for the compression of the magnetic field in the shock, are well below the observed ‘knee’ at $\sim 10^{15}$ eV in the Galactic cosmic-ray spectrum.

Subject headings: Supernova remnants — acceleration of particles — cosmic-rays — X-rays — radio — gamma-rays: ISM: individual (G347.3-0.5)

¹Department of Physics, North Carolina State University, Box 8202, Raleigh NC 27695, U.S.A.; E-mail: don_ellison@ncsu.edu

²Harvard Smithsonian Center for Astrophysics, 60 Garden Street, Cambridge, MA 02138, U.S.A.; E-mail: slane@cfa.harvard.edu

³Hubble Fellow

⁴Center for Space Research, Massachusetts Institute for Technology, Cambridge, MA 02139, U.S.A.; E-mail: bmg@space.mit.edu

1. INTRODUCTION

The supernova remnant G347.3–0.5 (ROSAT catalog source name: RX J1713.7–3946) is one of a growing number of supernova remnants (SNRs) showing nonthermal X-ray emission attributed to shock accelerated electrons.⁵ In some cases, the nonthermal emission is evidenced by continuum emission extending to ~ 10 keV or above, usually superimposed with weak lines, or, as with SN1006, G347.3–0.5, and G266.2–1.2, by a complete lack of line emission in the observed X-ray band.⁶ In all cases where the emission is not associated with a compact object, the nonthermal X-rays have been interpreted as synchrotron emission from shock accelerated TeV electrons (e.g., Mastichiadis & de Jager 1996; Allen et al. 1997; Tanimori et al. 1998; Reynolds & Keohane 1999). If this is true, the existence of these TeV electrons has important implications, not only for the production of cosmic rays, but also for the thermal properties of the shock heated, X-ray emitting gas in SNRs.

Here we compare broad-band observations of G347.3–0.5 with results from a model combining hydrodynamic simulations of SNR evolution (e.g., Blondin & Ellison 2001, and references therein) with nonlinear diffusive particle acceleration (e.g., Ellison, Berezhko, & Baring 2000). The observations combine new radio data from the Australia Telescope Compact Array (ATCA) with existing X-ray (Slane et al. 1999) and γ -ray data (Muraishi et al. 2000). Our broad-band comparison of observations and model fits is a powerful way to constrain model parameters, but uncertainties from directly comparing radio, X-ray, and γ -ray observations are unavoidable and should be kept in mind. In an attempt to limit errors from uncertainties in emission volumes, we only consider observations from the northwest portion of G347.3–0.5 where the center of the TeV γ -ray response function coincides with the brightest radio and X-ray emission.

Previous work (e.g., Reynolds 1998) indicates that the steepness of the nonthermal X-ray synchrotron spectrum in shell-like SNRs results because these photons are generated by electrons in the steeply falling, high-energy tail of the distribution. The actual maximum electron energy, however, depends on the magnetic field strength, B_2 , in the emission region. If these electrons are accelerated by the first-order Fermi shock acceleration mechanism as we assume, it is almost certain that the same shocks accelerate ions, but no clear evidence of superthermal ions has yet been obtained (i.e., no pion-decay feature has been unambiguously identified at ~ 100 MeV in SNRs). Until a pion-decay feature is observed, all information on the energetic ions must be obtained through modeling. In shocks accelerating particles efficiently, the unseen ions dominate the shock dynamics and largely control the electron emission features (e.g., Drury 1983; Jones & Ellison 1991).

⁵As of this writing, the list of SNRs with nonthermal X-ray emission associated with shock acceleration rather than, or in addition to, pulsar-powered emission includes: Tycho, Kepler, Cas A, SN1006, G266.2–1.2, G347.3–0.5, RCW 86, G156.2+5.7, and 3C397.

⁶SN1006 shows line emission from the central regions, but nearly featureless spectra from the bright rim (e.g., Koyama et al. 1995).

Our main results are: (i) A spherically symmetric, wind-shell model with efficient acceleration can produce broad-band continuum spectra in excellent agreement with the observations of G347.3–0.5; (ii) Test-particle models of G347.3–0.5 (i.e., ones where less than a few percent of the total energy ends up in relativistic particles) can be excluded with good confidence; (iii) The maximum electron energy in G347.3–0.5 is well below 10^{14} eV. Thus, G347.3–0.5 joins several other SNRs now known *not* to produce electrons above 10^{14} eV (e.g., Reynolds & Keohane 1999), well below the so-called knee in the Galactic cosmic-ray spectrum at $\sim 10^{15}$ eV. The maximum proton energy depends somewhat on whether or not the ambient magnetic field is compressed by the shock. If the field is compressed as the density, the maximum proton energy is approximately the same as the electron E_{max} . In the other extreme, where no compression of the field occurs, we find that G347.3–0.5 could currently be producing protons to ~ 70 TeV and Fe^{+26} to $\sim 10^{15}$ eV. Unless substantial magnetic field amplification occurs, G347.3–0.5 will not produce higher energy protons as it ages; and (iv) Our main conclusions concerning maximum particle energies and acceleration efficiency, are relatively insensitive to uncertainties stemming from the morphology of G347.3–0.5.

There are strong arguments for a SNR origin of cosmic rays based mainly on ion composition (e.g., Ellison, Drury, & Meyer 1997; Meyer, Drury, & Ellison 1997) and total energy requirements (e.g., Axford 1981; Blandford & Eichler 1987; Drury, Markiewicz, & Völk 1989). The observations of nonthermal X-ray emission showing that TeV electrons are produced in SNRs adds support for this argument. However, there is still no direct evidence that ions are generated in particular SNRs in a fashion consistent with cosmic-ray observations. The low maximum proton energy inferred for G347.3–0.5 may present a problem for the scenario that SNRs are the main sources of Galactic cosmic rays below the knee and suggest that the cosmic-ray proton component above $\sim 10^{14}$ eV might come from some subset of SNRs substantially different from G347.3–0.5. Alternatively, young SNRs which only produce $\sim 10^{13}$ eV particles when they are bright in X-rays, may somehow be able to produce higher energy particles at later times, perhaps by amplifying the magnetic field (e.g., Keohane, Gotthelf, & Petre 1998; Jun & Jones 1999; Lucek & Bell 2000). We note that the high magnetic fields inferred for Cas A make it likely that this particular remnant *does* produce $\sim 10^{15}$ eV protons (e.g., Allen et al. 1997).

2. Observations

G347.3–0.5 was observed with the *Advanced Satellite for Cosmology and Astrophysics* (ASCA) on 1997 March 25 for a total of 50 ks using three pointings of 10 ks duration and one (in the fainter southeast region) of 20 ks duration (Slane et al. 1999). Unlike the line-dominated X-ray spectra typical of SNRs, the spectrum for G347.3–0.5 is observed to be featureless and to extend to at least 10 keV, where the ASCA effective area becomes very small. A power law spectrum provides an excellent fit to the X-ray data, with some indication that the spectral index varies between the brighter shell regions and the more diffuse interior and eastern regions. The brightest X-ray emission occurs along the northwest limb of the SNR (see Figure 1), where there is some indication

that the remnant may be interacting with a molecular cloud or a stellar wind bubble shell, although the low inferred density for this region more likely indicates some density enhancement caused by a perturbation of the pre-SN wind. The unabsorbed flux density from this region of the remnant is $F_x(0.5 - 10 \text{ keV}) = 1.6 \times 10^{-10} \text{ erg cm}^{-2} \text{ s}^{-1}$ with a power law photon index of $2.41^{+0.05}_{-0.04}$.

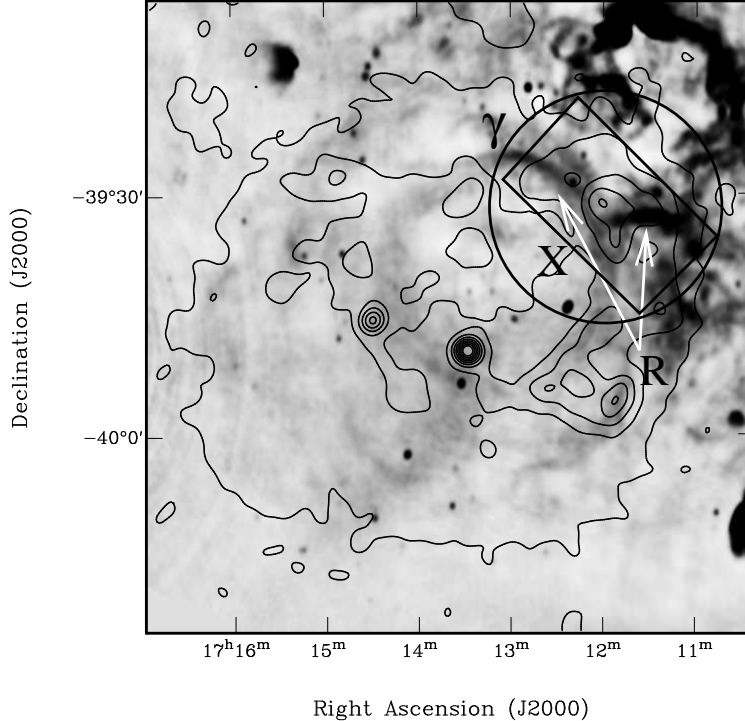


Fig. 1.— G347.3-0.5 at 1.36 GHz, from the ATCA, with X-ray contours from the ROSAT PSPC (Pfeffermann & Aschenbach 1996). The modeling presented here corresponds to emission from the northwest limb of the SNR. The radio flux used for our modeling is from the two bright filaments indicated with white arrows. The X-ray spectrum was extracted from the region indicated by a box. The circle on the figure is placed at the centroid of the γ -ray emission detected by the CANGAROO telescope; the radius of the circle corresponds to the telescope point response function.

Described here are new radio observations of G347.3-0.5 made with the Australia Telescope Compact Array (ATCA), a six-element synthesis telescope located near Narrabri, NSW, Australia. Observations at 1.36 GHz were carried out in January, March, and April 1998, in each case in a different array configuration to give maximal $u - v$ coverage. The field was imaged in a 10-point mosaic, to ensure that the entire extent of the SNR, as well as nearby bright sources, were in the field-of-view. The interferometric visibilities were edited to remove corrupted data and interference. Calibrations were then applied to solve for the time-variable atmospheric gains above each antenna and for the polarization leakage in the receivers. An absolute flux density scale was applied to the data using observations of PKS B1934-638, for which a flux density of 15.0 Jy was assumed at a frequency of 1.4 GHz. The visibilities from all 10 pointings were then inverted to

produce a single image, which was deconvolved using the mosaiced maximum entropy approach described by Sault, Staveley-Smith, & Brouw (1996). The final image was then produced by applying a Gaussian restoring beam of dimensions $46'' \times 36''$. The sum of the flux from the two bright filaments in the northwest region of the remnant (indicated in Figure 1 and labeled as arc 1 and 2 in Slane et al. 1999), corresponding to that from which the X-ray flux above was measured, is $S(1.36 \text{ GHz}) = 4 \pm 1 \text{ Jy}$. As noted in Slane et al. (1999), while arc 2 (the right-most arc in Figure 1) is askew from the perceived SNR shell, it does overlap an X-ray filament. Arcs 1 and 2 have approximately the same radio flux.

G347.3-0.5 has also been detected at TeV energies with the CANGAROO 3.8m atmospheric imaging Čerenkov telescope (Muraishi et al. 2000). As with the X-ray and radio observations, the $\sim 5.6\sigma$ detection is from the NW rim of the remnant (indicated with a circle in Figure 1) and has an estimated flux of $5.3 \pm 0.9[\text{statistical}] \pm 1.6[\text{systematic}] \times 10^{-12} \text{ photons cm}^{-2} \text{ s}^{-1}$ at energies $\geq 1.8 \pm 0.9 \text{ TeV}$.

The fluxes from these three detections are shown in Figures 3 and 4 where we have increased the observational error bars on the radio and TeV points by a factor of two (light-weight bars) to compensate for uncertainties in the relative emission volumes. In particular, the increased radio error bar will accommodate the possibility that arc 2 is not associated with the SNR shell and thus none of our results will change if this is the case.

3. Model

3.1. Nonlinear diffusive shock acceleration

Collisionless shocks are known to accelerate particles efficiently. In the heliosphere, where shocks are observed directly with spacecraft, there is clear evidence that the quasi-parallel earth bow shock (with a sonic Mach number, $M_{S0} < 10$) can place 10-30% of the solar wind kinetic energy flux into superthermal particles (e.g., Ellison, Möbius, & Paschmann 1990). Interplanetary shocks (IPSs) also accelerate ambient particles but generally with lower efficiencies due to their lower Mach numbers (generally $M_{S0} \lesssim 3$ for IPSs) (e.g., Baring et al. 1997). However, on at least two occasions, exceptionally strong IPSs have been observed to accelerate particles with high efficiency (Eichler 1981; Terasawa et al. 1999). Hybrid plasma simulations showing direct injection and acceleration of ambient particles are consistent with these observations (e.g., Scholer, Trattner, & Kucharek 1992), as are convection-diffusion models (e.g., Kang & Jones 1997).

Compared to shocks in the heliosphere, it might be presumed that the strong forward and reverse shocks in young SNRs are much more efficient. As far as we can tell, there are no important differences in typical plasma parameters (i.e., density, magnetic field, temperature, composition) between the solar wind and the ambient ISM. The only real differences come from the much larger shock spatial and time scales and much higher flow speeds and Mach numbers in SNRs. In general,

these factors should increase the acceleration efficiency substantially over heliospheric shocks, but some qualifications must be made.

At quasi-parallel shocks (those where the upstream magnetic field makes an angle, Θ_{Bn} , of less than about 45° with the shock normal), injection from the shocked heated plasma should occur easily and the fraction of incoming ram kinetic energy flux going into superthermal particles increases with Mach number and shock size and/or age (as measured in particle gyroradii or gyroperiods). If however, the fraction of shocked heated particles injected is small enough, high Mach number, test-particle solutions can result (see Berezhko & Ellison 1999). In quasi-perpendicular shocks (ones where $45 < \Theta_{\text{Bn}} \lesssim 90^\circ$), injection and acceleration of shock heated thermal particles is suppressed above some Mach number unless strong turbulence is present (see Ellison, Baring, & Jones 1996, for example). Highly oblique interplanetary shocks are observed to accelerate the ambient solar wind (even without pickup ions, Ellison, Jones, & Baring 1999), but these are low Mach number shocks. As the Mach number increases, injection becomes more likely if the turbulence is strong enough for cross-field diffusion in the downstream plasma to be important.

While the shock obliquity will surely vary around a SNR and some portions of the shocks may be quasi-perpendicular with low injection rates, other regions should be parallel enough for efficient injection and acceleration to occur. Radio emission is a sure sign that relativistic electrons are present and flux levels, sharp radio edges, etc., show that these particles are locally accelerated in young SNRs rather than just compressed Galactic cosmic-ray electrons (e.g., Achterberg, Blandford, & Reynolds 1994). The shock acceleration and evolutionary models we use here ignore effects from oblique magnetic fields, other than those that are mimicked by a low injection efficiency. We do assume, however, that the magnetic field responsible for synchrotron radiation can be compressed by the shock. For a recent discussion of how the injection efficiency may vary with Θ_{Bn} in SNRs, see Völk (2001).

The nonlinear effects in efficient shock acceleration are of three basic kinds: (i) the self-generation of magnetic turbulence by accelerated particles, (ii) the modification (i.e., smoothing) of the shock structure by the backpressure of accelerated particles, and (iii) the increase in shock compression ratio as relativistic particles are produced and some high-energy particles escape from the system. Briefly, (i) occurs when counter-streaming accelerated particles produce turbulence in the upstream magnetic field which amplifies as it is convected through the shock. This amplified turbulence results in stronger scattering of the particles, and hence to more acceleration, quickly leading to saturated magnetic turbulence levels near $\delta B/B \sim 1$ in strong shocks. This is the so-called Bohm limit where the mean free path is of the order of the gyroradius, and in this limit, the distinction between parallel and oblique shocks blurs. The wave-particle interactions produce heating in the shock precursor which may be observable and which lowers the overall acceleration efficiency. Effect (ii) occurs because the accelerated population presses on the upstream plasma and slows it. An upstream precursor forms, in which the flow speed (in the shock frame and in the absence of instabilities) is monotonically decreasing. Since particle diffusion lengths are increasing functions of momentum, high momentum particles sample a broader portion of the

flow velocity profile, and hence experience larger effective compression ratios than low momentum particles. Consequently, higher momentum particles have a flatter power-law index than those at lower momenta (producing a concave upward spectral curvature) and can dominate the pressure in a non-linear fashion. We call the ratio of densities spanning the entire upstream precursor the overall compression ratio, r_{tot} , to distinguish it from the small scale subshock compression ratio, r_{sub} , where most of the shock heating occurs. For a more complete discussion of the nonlinear effects of diffusive shock acceleration, see Berezhko & Ellison (1999).

The conservation of mass, momentum, and energy fluxes, i.e., the Rankine-Hugoniot relations, yield the standard expression for the compression ratio in shocks where the magnetic field is not dynamically important and an insignificant fraction of energy is placed in superthermal particles (i.e., test-particle shocks):

$$r_{\text{tot}} = \frac{(\gamma + 1)M_{\text{S0}}^2}{(\gamma - 1)M_{\text{S0}}^2 + 2} , \quad (1)$$

where $M_{\text{S0}} = \sqrt{\rho_0 V_{\text{sk}}^2 / (\gamma P_0)}$ is the sonic Mach number, γ is the ratio of specific heats, ρ_0 is the unshocked density, P_0 the unshocked pressure, and V_{sk} is the shock speed.⁷ In test-particle shocks, $r_{\text{tot}} = r_{\text{sub}}$. The ratio of shocked to unshocked pressure follows:

$$\frac{P_2}{P_0} = \frac{2\gamma M_{\text{S0}}^2 - (\gamma - 1)}{\gamma + 1} . \quad (2)$$

If $M_{\text{S0}} \gg 1$,

$$r_{\text{tot}} \simeq \frac{\gamma + 1}{\gamma - 1} , \quad (3)$$

and

$$P_2 \simeq P_0 \frac{2\gamma M_{\text{S0}}^2}{\gamma + 1} = \frac{2\rho_0 V_{\text{sk}}^2}{\gamma + 1} . \quad (4)$$

For a electron-proton plasma where the downstream temperatures are equal, the post-shock proton temperature in this test-particle limit, T_{tp} , is:

$$T_{\text{tp}} \simeq \frac{1}{r_{\text{tot}}} \frac{m_p V_{\text{sk}}^2}{k(\gamma + 1)} , \quad (5)$$

where k is Boltzmann's constant and m_p is the proton mass.

Young SNR shocks are expected to have high Mach numbers and if the test-particle situation is assumed with $\gamma \simeq 5/3$, we expect $r_{\text{tot}} \simeq 4$. However, when shocks accelerate particles the overall compression ratio increases above test-particle values (even in non-radiative shocks) for two reasons (effect iii above). First, as relativistic particles are produced and contribute significantly to the total pressure, their softer equation of state makes the shocked plasma more compressible ($\gamma \rightarrow 4/3$). Second, and most important, is that particles escape from strong shocks draining energy flux which

⁷Here and elsewhere, the subscript ‘0’ indicates unshocked values and the subscript ‘2’ indicates shocked values.

must be compensated for by ramping up the overall compression ratio to conserve the fluxes.⁸ Just as in radiative shocks, this is equivalent to $\gamma \rightarrow 1$. For strong injection, it can be shown (Berezhko & Ellison 1999) that r_{tot} is an ever increasing function of Mach number, i.e.,

$$r_{\text{tot}} \simeq \begin{cases} 1.3 M_{\text{S0}}^{3/4} & \text{if } 1 \ll M_{\text{S0}}^2 \ll M_{\text{A0}} ; \\ 1.5 M_{\text{A0}}^{3/8} & \text{if } 1 \ll M_{\text{A0}} < M_{\text{S0}}^2 , \end{cases} \quad (6)$$

where M_{A0} is the Alfvén Mach number (see also, Kazanas & Ellison 1986; Malkov 1997). Simultaneously with r_{tot} increasing, the subshock compression ratio, r_{sub} , which is mainly responsible for heating the gas, must drop below the test-particle value. Thus, high compression ratios are accompanied by low post-shock temperatures (in efficient shocks, the post-shock proton temperature can easily be $1/10 T_{\text{tp}}$).⁹ If injection is weak enough, however, equation (6) does not apply and high Mach number shocks do not accelerate enough particles to cause the total compression ratio to increase above ~ 4 (see Berezhko & Ellison 1999, for the parameters describing this condition).

The most important parameters associated with nonlinear shock acceleration are the Mach numbers (i.e., the shock speed, V_{sk} , pre-shock hydrogen number density, and preshock magnetic field, B_0), the injection efficiency, $\eta_{\text{inj,p}}$ (i.e., the fraction of total protons which end up with superthermal energies), and the maximum proton energy produced, $E_{\text{max,p}}$. As described in Berezhko & Ellison (1999), our model includes Alfvén heating in the precursor which reduces the efficiency compared to adiabatic heating.

We refer the reader to Ellison, Berezhko, & Baring (2000) for a discussion of our treatment of electron injection and acceleration.

3.2. SNR Evolution and Model Parameters

Slane et al. (1999) suggest that the forward shock of G347.3–0.5 is still within the pre-SN stellar wind bubble with part of it interacting with denser material. We describe this evolution with a spherically symmetric, wind-shell model with a pre-SN density distribution as shown in the top panel of Figure 2. The initial density profile in the ejecta has a power law distribution, $\rho \propto r^{-n}$, with a constant density plateau at small radii, as described in Chevalier (1982a). Since we only consider the forward shock at fairly late stages in the SNR evolution, our results are insensitive to n and the position of the plateau. They are also insensitive to whether a power-law or exponential ejecta mass density distribution (e.g., Dwarkadas & Chevalier 1998) is assumed. For concreteness,

⁸As long as the speeds of the escaping particles are much greater than the shock speed, escaping momentum and mass fluxes can be neglected (Ellison 1985).

⁹Hughes, Rakowski, & Decourchelle (2000) have used this effect to reconcile the high values of the shock speed determined from expansion measurements and the low post-shock electron temperature determined from X-ray line models in SNR E0102.2-7219.

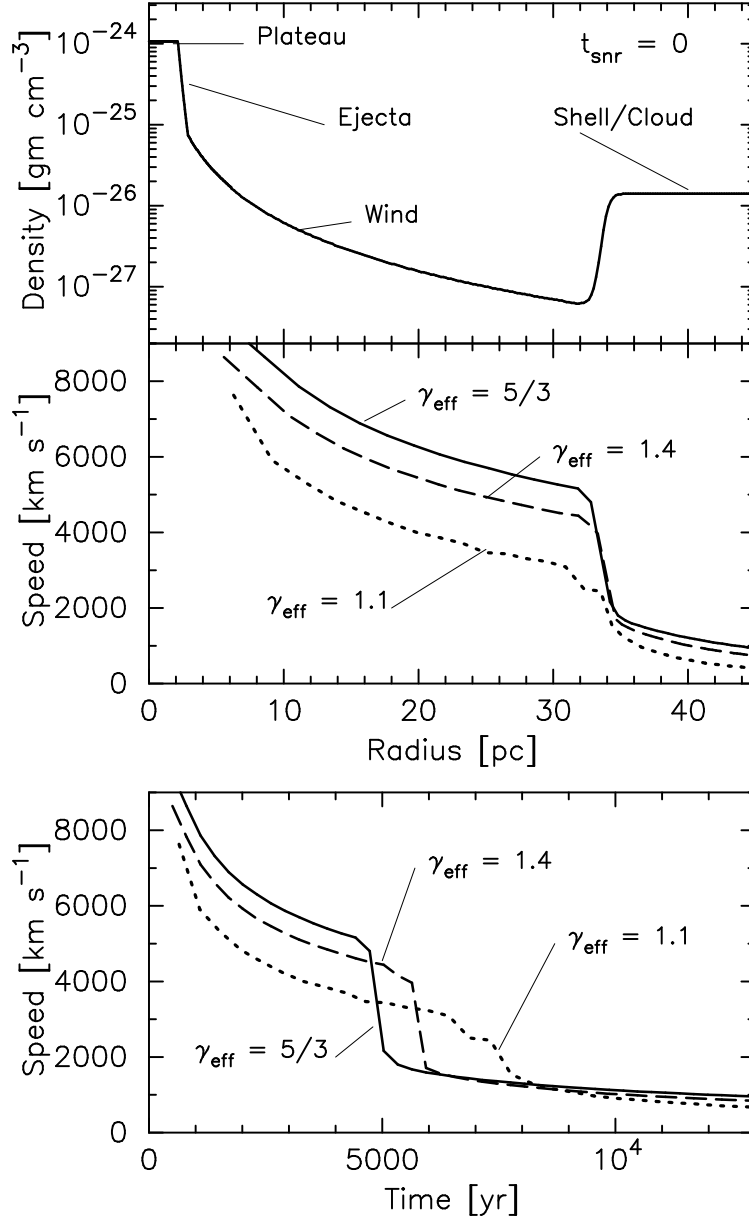


Fig. 2.— The top panel shows a snapshot of a typical density profile at the start of the hydrodynamic simulation (i.e., at $t_{\text{snr}} = 0$). The spatial scale assumes that G347.3–0.5 has a diameter of $\sim 45'$ and is 6 kpc away. The inner edge of the shell is at ~ 34 pc and the current radius of the forward shock is at ~ 40 pc. The middle panel shows the evolution of the forward shock speed as a function of radius and the bottom panel shows the shock speed as a function of remnant age. The different curves in the lower two panels were obtained by running the hydro code with the indicated effective ratios of specific heats. In all cases, the speed drops sharply as the forward shock enters the shell.

we use $n = 9$ in all of our models. As in Chevalier (1982b), the density of the pre-SN wind is given by

$$\rho_w = A_0 r^{-2} , \quad (7)$$

where $A_0 = dM_{\text{loss}}/dt/(4\pi v_w)$, dM_{loss}/dt is the pre-SN mass loss rate, and v_w is the constant wind speed. At some distance from the explosion, we place a shell of uniform density, $\rho_{\text{shell}} = m_p n_{\text{shell}} (1 + 4 f_\alpha)$ — our spherically symmetric representation of the density enhancement suggested by Slane et al. (1999). Here, $f_\alpha = 0.1$ is the number fraction of helium and n_{shell} is the proton number density in the shell. While the radio image of G347.3–0.5 suggests a shell with the strongest emission coming from the NW rim, the complex morphology makes an exact determination of the diameter somewhat ambiguous. Some radio and X-ray emission extends across $\sim 60'$, but a smaller $\sim 30'$ diameter ring-like structure is also present. As a compromise, we adopt an angular diameter of $45'$, and to further limit parameters, we perform all of our fits assuming a distance of $D_{\text{snr}} = 6$ kpc (Slane et al. 1999). With these assumptions, the outer shock is at a radius $R_{\text{sk}} \sim 40$ pc and we take (somewhat arbitrarily) the inner radius of the shell to be $R_{\text{in}} \sim 34$ pc, giving a shell thickness approximately equal to the thickness of radio arc 1, i.e., $(R_{\text{sk}} - R_{\text{in}})/R_{\text{sk}} \sim 3'/22.5'$. Fortunately, none of our conclusions depend critically on these particular values. Furthermore, as long as $\rho_w(R_{\text{in}}) \ll \rho_{\text{shell}}$, our results are insensitive to A_0 and we use $A_0 = 6 \times 10^{12} \text{ gm cm}^{-1}$ which is consistent with a wind extending to 34 pc.¹⁰

The evolution is calculated with the Virginia Hydrodynamics (VH-1) time-dependent hydrodynamic numerical code in one dimension where it is implicitly assumed that dynamic effects from magnetic fields are negligible. For a description of this code, see Blondin & Ellison (2001) and references therein. With the shock speed and other parameters obtained with the hydro code, we calculate the electron, proton, and helium spectra and with them the synchrotron, bremsstrahlung, inverse-Compton, and pion-decay photon continuum spectra. We then compare the photon emission to the observations and vary parameters until a satisfactory fit is obtained.

3.2.1. Approximations of the wind-shell model

Of necessity, our model is approximate in some important ways. First, we assume the SNR is spherically symmetric when, in fact, the emission is strongest from one section of the rim where the shock is likely interacting with denser material. We compensate for this at the most basic level by defining the emission volume, V_{emis} , as a fraction, f_{vol} , of the shell volume encompassed by the forward shock, i.e.,

$$V_{\text{emis}} = f_{\text{vol}} \left(\frac{4\pi}{3} \right) (R_{\text{sk}}^3 - R_{\text{in}}^3) . \quad (8)$$

¹⁰For $dM_{\text{loss}}/dt = 7 \times 10^{-6} M_\odot \text{ yr}^{-1}$ and $v_w = 60 \text{ km s}^{-1}$ (giving $A_0 = 6 \times 10^{12} \text{ gm cm}^{-1}$), $\sim 4M_\odot$ would exist in a spherical wind extending to 34 pc. With this v_w , the wind bubble would have taken $\sim 6 \times 10^5 \text{ yr}$ to form and could still not have stagnated in a low density interstellar medium.

From Figure 1 we estimate that $0.05 < f_{\text{vol}} < 0.25$.

Second, we use a one-zone model where the particle spectra and photon emission are assumed to be generated by a shock of constant speed during the time the forward shock is in the shell. We ignore any evolution of the spectra or the shock during the time the shock is in the shell and the shock speed used for acceleration is the average speed in the shell as determined by the hydro code. Furthermore, we neglect any contributions from the reverse shock or reflected shocks which occur when the forward shock enters the shell. These should be excellent approximations since the forward shock speed doesn’t vary greatly while in the shell (middle panel Figure 2), particles produced earlier in the low density wind or ejecta have been reduced by adiabatic losses, and reflected shocks in the shell are weak compared to the forward shock.

The evolution of the SNR will be influenced by the acceleration process through the increased compression ratios of the forward and reverse shocks and by the escape of high energy cosmic rays. We have approximated this effect by performing our hydrodynamic calculations with values of the effective ratio of specific heats, $\gamma_{\text{eff}} \leq 5/3$, as described in detail in Blondin & Ellison (2001). The effect on the forward shock speed is shown for typical parameters in the bottom panel of Figure 2. The solid curve is for $\gamma_{\text{eff}} = 5/3$ ($r_{\text{tot}} \simeq 4$), the dashed curve is for $\gamma_{\text{eff}} = 1.4$ ($r_{\text{tot}} \simeq 6$), and the dotted curve is for $\gamma_{\text{eff}} = 1.1$ ($r_{\text{tot}} \simeq 20$). When $\gamma_{\text{eff}} = 5/3$, the shock reaches 40 pc after $t_{\text{snr}} \sim 1.3 \times 10^4$ yr, for $\gamma_{\text{eff}} = 1.4$, it reaches 40 pc after $\sim 1.45 \times 10^4$ yr, and for $\gamma_{\text{eff}} = 1.1$, 40 pc is reached after $\sim 1.8 \times 10^4$ yr. While globally changing γ_{eff} only approximates the effects of particle acceleration on the evolution (particle escape is not explicitly included and the evolution of γ_{eff} is not modeled, for example), we do not believe errors from this approximation are significant since all of the models we discuss below have compression ratios less than ~ 6 when the forward shock is in the shell. As indicated in Figure 2, at $R_{\text{sk}} = 40$ pc V_{sk} varies by less than 25% for $r_{\text{tot}} \leq 6$. Despite this small change in V_{sk} , the particle spectra produced by a shock with $r_{\text{tot}} = 6$ are still strongly nonlinear and differs importantly from test-particle spectra as shown in the fits below.

Finally, our model ignores X-ray *line* emission which, for a thermal plasma, can be much more intense than the pure bremsstrahlung component. For example, the 0.2–10 keV flux for a $kT = 0.2$ keV Raymond-Smith model (Raymond & Smith 1977) is ~ 20 times higher than for a thermal bremsstrahlung model with the same temperature and emission measure. This discrepancy decreases with temperature, dropping to ~ 4 at $kT = 1$ keV and ~ 1.4 at $kT = 2.5$ keV. If the featureless X-ray spectrum in G347.3–0.5 is synchrotron emission, the underlying bremsstrahlung continuum which we calculate must be low enough so lines, had they been calculated, would not appear.

3.2.2. Model parameters

Most of the parameters used in our models are described in Ellison, Berezhko, & Baring (2000) and/or shown here in Table 1. Briefly: (i) The explosion energy, E_{sn} , largely determines the overall

dynamics and is typically assumed to be near 10^{51} erg. The ejecta mass, M_{ej} , is unimportant for the ages and parameters we consider as long as it is less than about $3 M_{\odot}$. If $M_{\text{ej}} \gtrsim 3 M_{\odot}$, the reflected shock produced when the forward shock enters the shell can interact with the density peak behind the reverse shock producing complicated flow structures. To avoid these complications, we limit consideration to $M_{\text{ej}} < 3 M_{\odot}$ and do not list this parameter in the Table. (ii) The magnetic field affects the particle acceleration and largely determines the shape of the broad-band photon emission through its influence on synchrotron emission. The field morphology is certain to be complex in any real SNR and will vary with location (see Jun & Jones 1999, for an excellent 2-D MHD study of shock-cloud interactions). To consider a range of possibilities in our idealized, spherically symmetric model, we assume the downstream field, B_2 , is either equal to the upstream (unshocked) field, i.e., $B_2 = B_0$, or that B_2 is compressed along with the gas, i.e., $B_2 = r_{\text{tot}} B_0$. The actual situation should lie somewhere in between. We assume the unshocked proton temperature, $T_{p0} = 10^4 \text{ K} = T_{e0} = T_{\alpha 0}$, where T_{e0} ($T_{\alpha 0}$) is the upstream electron (helium) temperature. Our solutions are insensitive to the upstream temperature as long as it is below $\sim 10^6 \text{ K}$. The shocked electron to proton temperature ratio, T_{e2}/T_{p2} , is a free parameter which has not yet been deduced from first principles for collisionless shocks. The electron temperature is an important parameter for thermal bremsstrahlung and X-ray line emission, but is not strongly constrained for G347.3–0.5 because no lines are seen. In any case, we assume $T_{e2}/T_{p2} = 1$ in all of our models but note that if electron-proton equilibration timescales are long compared to dynamic timescales, T_{e2}/T_{p2} could be considerably less than one, lowering the thermal bremsstrahlung to synchrotron ratio.¹¹ (iii) The injection efficiency, $\eta_{\text{inj,p}}$, is the fraction of thermal protons that end up as accelerated particles. This parameter influences the overall acceleration efficiency. (iv) The electron to proton ratio at relativistic energies, $(e/p)_{\text{rel}}$, is an arbitrary parameter in our models but is expected to lie between 0.01 and 0.05 if $(e/p)_{\text{rel}}$ in Galactic cosmic rays is typical of that produced by the strong shocks in young SNRs. This factor influences the normalization of the photon emission from electrons and is important for determining the pion-decay contribution to TeV γ -rays relative to inverse-Compton. The maximum energy cosmic rays obtain depends on the scattering mean free path, λ , which is assumed to be,

$$\lambda = \eta_{\text{mfp}} r_{\text{g,max}} (r_{\text{g}}/r_{\text{g,max}})^{\alpha} , \quad (9)$$

where η_{mfp} is a constant, $r_{\text{g}} = p/(qB)$ is the gyroradius in SI units, $r_{\text{g,max}}$ is the gyroradius at the maximum momentum, p_{max} , and α is a constant parameter. Small values of η_{mfp} imply strong scattering and allow higher maximum proton energies in a given system. We use the Bohm limit ($\eta_{\text{mfp}} = 1$) in all of our models and note that while good fits to the observations can be obtained with larger η_{mfp} , these models will have similar acceleration efficiencies with *lower* proton maximum energies than the models we show. (v) Finally, n_{shell} is the proton number density in the shell which models the density enhancement presumed to exist in the NW rim. Slane et al. (1999) conclude,

¹¹The combination of high post-shock density and low post-shock proton temperature means that electrons should equilibrate on a faster timescale in shocks undergoing efficient acceleration compared to those where little acceleration occurs (Decourchelle, Ellison, & Ballet 2000).

from the lack of thermal emission, that the mean density around the remnant is quite low. With large uncertainties, they estimate upper limits on the ambient density of $0.014\text{--}0.28 (D_{\text{snr}}/6 \text{ kpc})^{-1/2} \text{ cm}^{-3}$, with a higher upper limit ($< 1 (D_{\text{snr}}/6 \text{ kpc})^{-1/2} \text{ cm}^{-3}$) for the northwest rim.

The output values are also given in Table 1. The shock speed, V_{sk} , is the average obtained from the hydro simulation over the shell thickness between $R = 34$ and 40 pc. The age of G347.3–0.5 is unknown, but Slane et al. (1999) have used emission measures to estimate a range $2000 < t_{\text{snr}} < 40,000$ yr. The value in the Table is that necessary to yield an outer shock radius of $R_{\text{sk}} \sim 40$ pc consistent with an angular diameter $\sim 45'$ at a distance of 6 kpc. The time the shock spends between 34 pc and 40 pc is Δt_{sh} . Given V_{sk} and the density, temperature, and magnetic field in the shell, the sonic and Alfvén Mach numbers are determined. The above parameters allow the nonlinear shock model to determine r_{tot} , r_{sub} , and γ_{eff} , as well as the proton, electron, and helium spectra. Note that consistent values of r_{tot} and γ_{eff} are found by iterating the hydro simulation with the particle acceleration calculation. The shocked magnetic field is B_2 , and the shocked proton temperature is T_{p2} . The shocked proton temperature for the corresponding test-particle shock, T_{tp} , is also given.

The particle momentum distributions, $f(p)$, are calculated as in Ellison, Berezhko, & Baring (2000) with the turnover at the highest energies described by:

$$f(p) \rightarrow f(p) \exp \left[-\frac{1}{\alpha} \left(\frac{p}{p_{\text{max}}} \right)^\alpha \right]. \quad (10)$$

Here, α is the same as in Eqn. (9) and p_{max} is determined by setting the acceleration time equal to Δt_{sh} , or by setting the diffusion length of the highest energy particles equal to $1/10 R_{\text{sk}}$, whichever gives the lowest p_{max} (see Baring et al. 1999). It turns out that a relatively slow turnover (i.e., $\alpha \sim 0.5$) is required to obtain the proper X-ray slope and to join the radio and X-ray observations. A similar effect was required to match the intensity and shape of the X-ray observations in SN1006 (Reynolds 1998; Berezhko, Ksenofontov, & Petukhov 1999; Ellison, Berezhko, & Baring 2000), and we take $\alpha = 0.5$ in all of our models. The electron and proton energies corresponding to p_{max} are $E_{\text{max,e}}$ and $E_{\text{max,p}}$ respectively and are listed in the Table. The acceleration efficiency, ϵ_{rel} , is defined as,

$$\epsilon_{\text{rel}} = \frac{F_{\text{rel}} + F_{\text{esc}}}{(1/2)\rho_0 V_{\text{sk}}^3}, \quad (11)$$

where F_{rel} and F_{esc} are the fractions of energy flux in relativistic protons and escaping protons, respectively.

The spectral index at 2 GHz, where $F_\nu \propto \nu^\sigma$, is shown in the next to last row of Table 1. Radio data has been collected at 2.4 GHz from G347.3–0.5 but has not yet been analyzed. When the 2.4 GHz flux is combined with the existing 1.4 GHz flux, the inferred spectral index can be used as a check of our models and may help constrain parameters. Finally, the last row in the Table is the fraction of the shell volume, f_{vol} , producing the emission seen from the NW limb. Based on equation (8), models with $f_{\text{vol}} > 0.25$ are unacceptable.

Table 1: Forward shock parameters for G347.3–0.5. All models listed have $\eta_{\text{mfp}} = 1$, $\alpha = 0.5$, $T_{p0} = 10^4$ K, and $D_{\text{snr}} = 6$ kpc.

Input	A	B	C
$E_{\text{sn}} [10^{51} \text{ erg}]$	2	3	4
$B_0 [\mu\text{G}]$	2.4	2.4	16
$\eta_{\text{inj,p}}$	1×10^{-3}	5×10^{-6}	1×10^{-3}
$(e/p)_{\text{rel}}$	0.03	0.05	0.04
$n_{\text{shell}} [\text{cm}^{-3}]$	0.015	0.02	0.008
Output			
$V_{\text{sk}} [\text{km s}^{-1}]$	980	1100	2100
$t_{\text{snr}} [\text{yr}]$	9000	8000	5000
$\Delta t_{\text{sh}} [\text{yr}]$	5000	4700	2200
M_{S0}	60	70	130
M_{A0}	27	35	6.3
r_{tot}	6.1	4.1	4.3
r_{sub}	3.0	4.0	3.4
γ_{eff}	1.4	1.65	1.6
$B_2 [\mu\text{G}]$	15	9.6	16
$kT_{\text{p2}} [\text{keV}]$	0.33	1.2	3.4
$kT_{\text{tp}} [\text{keV}]$	1.0	1.2	4.5
$E_{\text{max,p}} [\text{TeV}]$	14	16	70
$E_{\text{max,e}} [\text{TeV}]$	14	16	32
ϵ_{rel}	0.55	0.03	0.20
$\sigma(2 \text{ GHz})$	−0.45	−0.51	−0.54
Flux			
f_{vol}	0.16	6.8	0.19

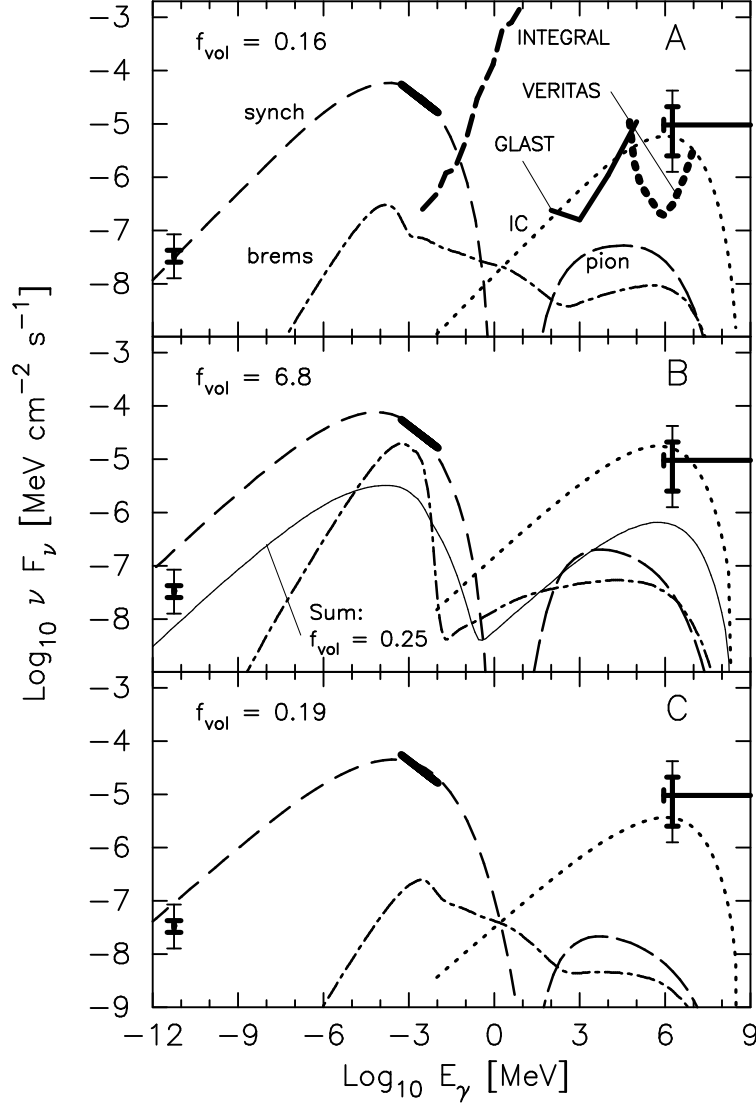


Fig. 3.— Comparison of broad-band emission from G347.3-0.5 with diffusive shock acceleration models. Model *A* uses a likely set of parameters with $B_2 = r_{\text{tot}} B_0$, model *B* is a fit obtained with a test-particle shock, and model *C* was obtained with parameters chosen to obtain the highest proton energy. In all panels, the short-dashed curves are synchrotron, the dot-dashed are bremsstrahlung, the dotted are inverse-Compton, the long-dashed curves are pion-decay, and the normalization is set by matching the synchrotron fluxes at ~ 5 keV. The heavy line at X-ray energies is the fit to the NW rim observations from Slane et al. (1999). The gamma-ray point is from Muraishi et al. (2000), and the radio data is first published here. The light-weight error bars on the radio and TeV points are included to compensate for the possible difference in relative emission volumes between the various energy bands. In the top panel we show the expected continuum sensitivity limits for the GLAST spacecraft (Gehrels & Michelson 1999), the INTEGRAL spacecraft (Winkler 1996), and the VERITAS array (Weekes et al. 1999). The solid curve in *B* is the total emission with $f_{\text{vol}} = 0.25$.

3.3. Fits to G347.3–0.5

The broad-band emission from G347.3–0.5 allows us to constrain the parameters of the shock model to fairly narrow ranges. In the top panel of Figure 3 (model *A*), we show a satisfactory fit to the broad-band observations with $B_2 = r_{\text{tot}} B_0$. The parameters for this model and two others discussed below are listed in Table 1. The four components of the emission are labeled and it’s clear that the synchrotron emission produces the radio and X-ray emission, while the TeV point is fit with inverse-Compton photons from electrons scattering off the 2.73 K background radiation. The value $f_{\text{vol}} = 0.16$ is consistent with the morphology and $n_{\text{shell}} = 0.015 \text{ cm}^{-3}$ is consistent with the upper limit estimate of Slane et al. (1999). We note that using a lower E_{sn} would force a smaller n_{shell} and a larger f_{vol} ; $E_{\text{sn}} > 1 \times 10^{51} \text{ erg}$ is clearly favored.

Using model *A* as a reference, we investigate how sensitive the fit is to particular parameters. In Figure 4 we show variations in B_0 , n_{shell} , E_{sn} , and $\eta_{\text{inj,p}}$. In each panel we keep all parameters except the one labeled fixed to the values used in model *A*. For all models, we have normalized the synchrotron emission to the flux in the X-ray band and plot the sum of the four photon components. The solid curve in each panel is model *A*. In the top panel, the dotted curve is for $B_0 = 1 \mu\text{G}$, the solid curve is for $B_0 = 2.4 \mu\text{G}$, and the dot-dashed curve is for $B_0 = 7 \mu\text{G}$. In all cases, the number in parentheses is f_{vol} . The dependence on B_0 is quite strong and the shape of the broad-band emission clearly sets upper and lower limits on B_0 . Furthermore, the $B_0 = 1 \mu\text{G}$ result can be excluded because $f_{\text{vol}} \simeq 4$; a low B produces too little flux.

The changes produced by varying n_{shell} are shown in the second panel of Figure 4. The dotted curve is for $n_{\text{shell}} = 0.005 \text{ cm}^{-3}$, the solid curve is for $n_{\text{shell}} = 0.015 \text{ cm}^{-3}$, and the dot-dashed curve is for $n_{\text{shell}} = 0.04 \text{ cm}^{-3}$. Clearly, the $n_{\text{shell}} = 0.005 \text{ cm}^{-3}$ result is too flat in the X-ray band, while the $n_{\text{shell}} = 0.04 \text{ cm}^{-3}$ result is somewhat too steep. The value $f_{\text{vol}} \simeq 1.1$ for $n_{\text{shell}} = 0.04 \text{ cm}^{-3}$, shows that this high density example produces too little flux. This occurs because V_{sk} is low in this case (520 km s^{-1}) producing a low $E_{\text{max,e}}$ and forcing a higher normalization to match the high energy X-rays.

In the third panel, we vary E_{sn} from $0.5 \times 10^{51} \text{ erg}$ (dotted curve) to $2 \times 10^{51} \text{ erg}$ (solid curve) to $4 \times 10^{51} \text{ erg}$ (dot-dashed curve). The low explosion energy gives an unacceptable fit because of the shape in the X-ray band and because $f_{\text{vol}} \simeq 8$. However, for $E_{\text{sn}} = 4 \times 10^{51} \text{ erg}$ the shape is still reasonably good considering the uncertainties in the model and the normalization ($f_{\text{vol}} \simeq 0.03$) while low, cannot be excluded.

In the bottom panel of Figure 4 we show results varying the injection efficiency. The dotted curve is for $\eta_{\text{inj,p}} = 10^{-5}$, the dot-dashed curve is for $\eta_{\text{inj,p}} = 10^{-4}$, and the solid curve is model *A* with $\eta_{\text{inj,p}} = 10^{-3}$. The shape of the sum of the emission is virtually identical for $\eta_{\text{inj,p}} = 10^{-4}$ and 10^{-3} . However, the intensity of the emission varies with $\eta_{\text{inj,p}}$ and for $\eta_{\text{inj,p}} = 10^{-4}$, $f_{\text{vol}} \simeq 0.3$, while for $\eta_{\text{inj,p}} = 10^{-3}$, $f_{\text{vol}} \simeq 0.16$. The constraint that the emission is only observed from a small fraction of the shell implies that $\eta_{\text{inj,p}} > 10^{-4}$. This will be true unless E_{sn} is considerably greater than $2 \times 10^{51} \text{ erg}$. The $\eta_{\text{inj,p}} = 10^{-5}$ result, which is what would be expected if the shock *did not*

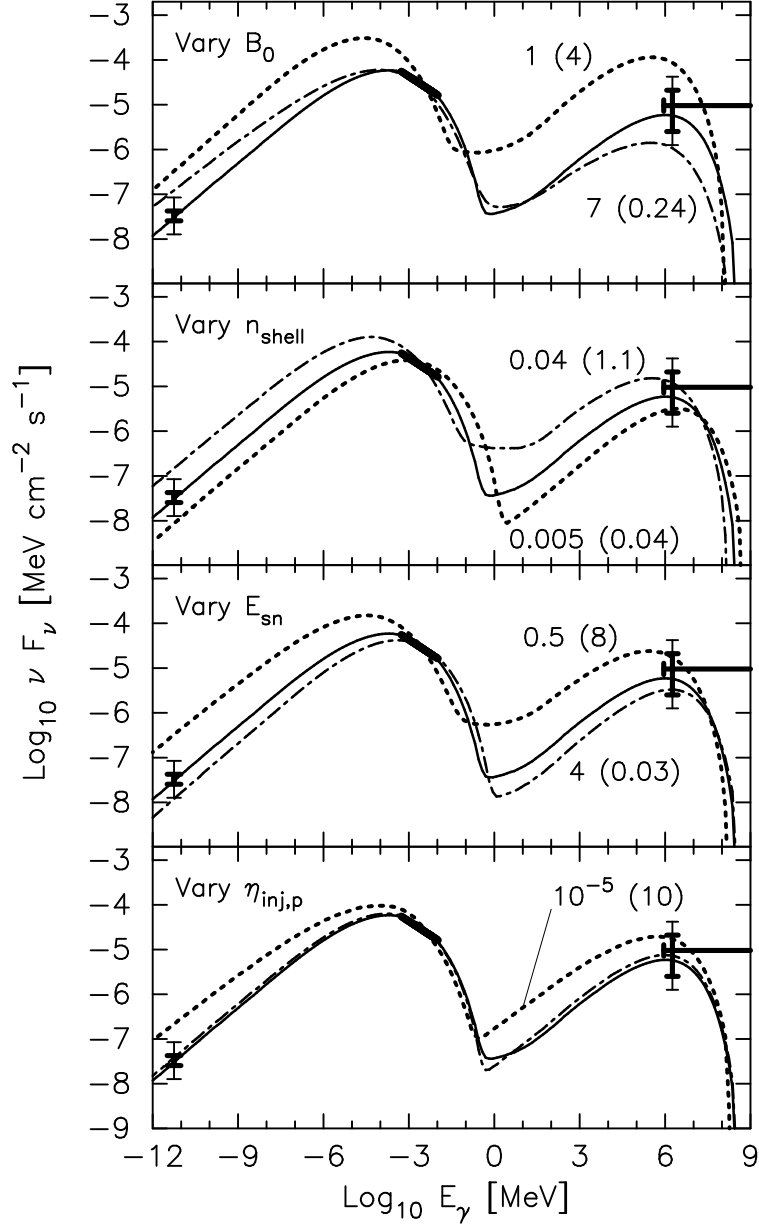


Fig. 4.— These plots and data are as in Figure 3 except here the curves are the sum of synchrotron, bremsstrahlung, inverse-Compton, and pion-decay emission. In each panel, the labeled parameter is varied as all other parameters are held fixed with the values shown in Table 1 for model A. The numbers in parentheses are f_{vol} . These models all have $B_2 = r_{\text{tot}} B_0$. In the bottom panel, $f_{\text{vol}} \simeq 10$ for $\eta_{\text{inj,p}} = 10^{-5}$ (dotted curve), $f_{\text{vol}} \simeq 0.3$ the $\eta_{\text{inj,p}} = 10^{-4}$ (dot-dashed curve), and $f_{\text{vol}} \simeq 0.16$ for $\eta_{\text{inj,p}} = 10^{-3}$ (solid curve).

accelerate particles efficiently, is unacceptable because of the overall shape and low emissivity (i.e., $f_{\text{vol}} \simeq 10$).

To further investigate the limits on the acceleration efficiency, we choose $\eta_{\text{inj,p}}$ low enough so only a few percent of the total energy flux ends up in relativistic particles and freely adjust other parameters to obtain a fit. With $\eta_{\text{inj,p}} = 5 \times 10^{-6}$ (yielding $\epsilon_{\text{rel}} \sim 3\%$) we are able to obtain an approximate match to the shape of the observed emission with Model *B* in Figure 3 and Table 1. Note that this model requires $E_{\text{sn}} = 3 \times 10^{51}$ erg; lower energies give poorer fits. While the shape of the continuum emission is a reasonable match to the observations, the normalization requires $f_{\text{vol}} \sim 6.8$, well above an acceptable value. Furthermore, the synchrotron emission from the test-particle shock is somewhat too steep to simultaneously match the radio and X-ray fluxes, and the ratio of synchrotron to bremsstrahlung continuum emission in the X-ray range is less than a factor of 3. If we further decrease $\eta_{\text{inj,p}}$, the synchrotron to bremsstrahlung ratio will drop and at some point X-ray emission lines would stand above the continuum flux in conflict with the observations. This conclusion depends, of course, on $T_{\text{e2}}/T_{\text{p2}}$ and could be weakened by assuming $T_{\text{e2}}/T_{\text{p2}} \ll 1$. However, the relative acceleration efficiency of electrons and protons is also likely to scale as $T_{\text{e2}}/T_{\text{p2}}$ (Ellison, Berezhko, & Baring 2000) making it difficult to produce the observed radio and TeV flux if $T_{\text{e2}}/T_{\text{p2}}$ is too small. Furthermore, if a flatter synchrotron slope is required to give a better match between the radio and X-rays (as in model *A*), this forces the shock to be more efficient (to produce a larger r_{tot}) and implies a larger $\eta_{\text{inj,p}}$. The overall flux, the lack of X-ray emission lines, and the radio to X-ray flux ratio all point toward efficient shock acceleration. Using this model we can get a firm lower limit on the acceleration efficiency by increasing $\eta_{\text{inj,p}}$ until $f_{\text{vol}} \sim 0.25$. We find $f_{\text{vol}} \lesssim 0.25$ for $\eta_{\text{inj,p}} > 3 \times 10^{-5}$, yielding a lower limit $\epsilon_{\text{rel}} > 0.25$, i.e., even with $E_{\text{sn}} = 3 \times 10^{51}$ erg, the shock must place at least 25% of its kinetic energy flux in relativistic particles. Note that we took $(e/p)_{\text{rel}} = 0.05$ for this example. A lower $(e/p)_{\text{rel}}$ would imply a higher acceleration efficiency.

In order to investigate the maximum proton energies that G347.3–0.5 can generate, we have produced Model *C* (bottom panel of Figure 3) where we have chosen parameters (including taking $B_2 = B_0$) with the intention of maximizing $E_{\text{max,p}}$. Very generally, diffusive shock acceleration yields the same maximum energy per *charge* for all particles (e.g., Drury 1983; Baring et al. 1999), so the only way the proton and electron spectra can have different maximum energies is for losses (synchrotron and/or inverse-Compton) to be important for the electrons. Unless we have neglected an abundant supply of photons in addition to the 2.73 K background radiation, inverse-Compton losses are not important and only when the magnetic field is large can $E_{\text{max,p}}$ be much greater than $E_{\text{max,e}}$. However, a large field produces a lower Alfvén Mach number which weakens the acceleration and, in order to fit the broad-band spectrum, a higher shock speed is required. This can be achieved with a larger E_{sn} and/or a lower n_{shell} , and we have taken $E_{\text{sn}} = 4 \times 10^{51}$ erg and $n_{\text{shell}} = 0.008 \text{ cm}^{-3}$ for Model *C*. The observed radio flux sets the strength of the magnetic field in the emission region combined with the relativistic electron density, i.e., the flux is loosely

proportional¹² to $B_2^{3/2} n_e$. Furthermore, the TeV inverse-Compton emission comes from the same electrons that produce the X-rays. Since the inverse-Compton emission is independent of B , it constrains the number of relativistic electrons. The combination of these constraints allows us to limit $E_{\text{max,p}}$ and we find in our most optimistic case that $E_{\text{max,p}} \lesssim 70$ TeV.

In Figure 5 we show the momentum distribution functions, $f(p)$, for models A , B , and C , where we have plotted the dimensionless quantity, $p^4 f(p)/(m_p c n_{p0})$, to emphasize the spectral curvature. In this representation, the test-particle result of $f(p) \propto p^{-4}$ is a horizontal line (model B). The concave shape of $f(p)$ (at superthermal energies and below the cutoff) is evident for models A and C , as is the large difference between the relativistic particle populations in these shocks with efficient acceleration compared to the inefficient shock B . As noted above, a flat electron spectrum (at energies greater than $m_p c^2$) produced by a large r_{tot} ($r_{\text{tot}} \simeq 6$ in model A) allows a good match between the radio and X-ray observations.

The arrows in Figure 5 indicate the positions of $E_{\text{max,p}}$ and $E_{\text{max,e}}$ as determined from equation (10) with $\alpha = 0.5$. In all cases, $f(p)$ starts to fall off exponentially at momenta less than p_{max} and much below $p = 10^6 m_p c$. Furthermore, if G347.3-0.5 continues to evolve uniformly with no magnetic field amplification, it will not produce higher energy particles as it ages (for a more complete discussion of the time particles take to obtain their maximum energies, see Berezhko & Völk 1997, 2000). Since the causes of magnetic field amplification are still uncertain, it remains possible that higher fields and therefore higher energy particles could be produced in the future. Magnetic field amplification apparently occurs in Cas A (e.g., Gull 1975; Keohane, Gotthelf, & Petre 1998) but if it is due to Rayleigh-Taylor instabilities in this young remnant as commonly assumed, it is unlikely that this mechanism would occur in G347.3–0.5, which is much older.

4. Conclusions

G347.3-0.5 is one of a growing number of shell-type SNRs showing nonthermal X-rays believed produced by synchrotron emission from TeV electrons accelerated by the remnant shocks. In an attempt to have a consistent, broad-band spectrum, we have combined recent X-ray and TeV γ -ray observations of the remnant with new radio observations and have restricted all of the observations to the bright northwest rim of the shell. Comparing a spherically symmetric, wind-shell model of SNR evolution and efficient diffusive shock acceleration against the observations shows that the observed emission can be well fit across ~ 18 decades in energy with a single set of parameters all close to expected supernova and ISM values. The densities we find for the emission region (~ 0.01 protons cm^{-3}) are consistent with the upper limits found earlier by Slane et al. (1999), and are below those expected for either a molecular cloud or a swept-up shell produced as the pre-SN wind

¹²This is not a strict proportionality because changing either B or the density produces changes in the acceleration model and/or the SNR evolution.

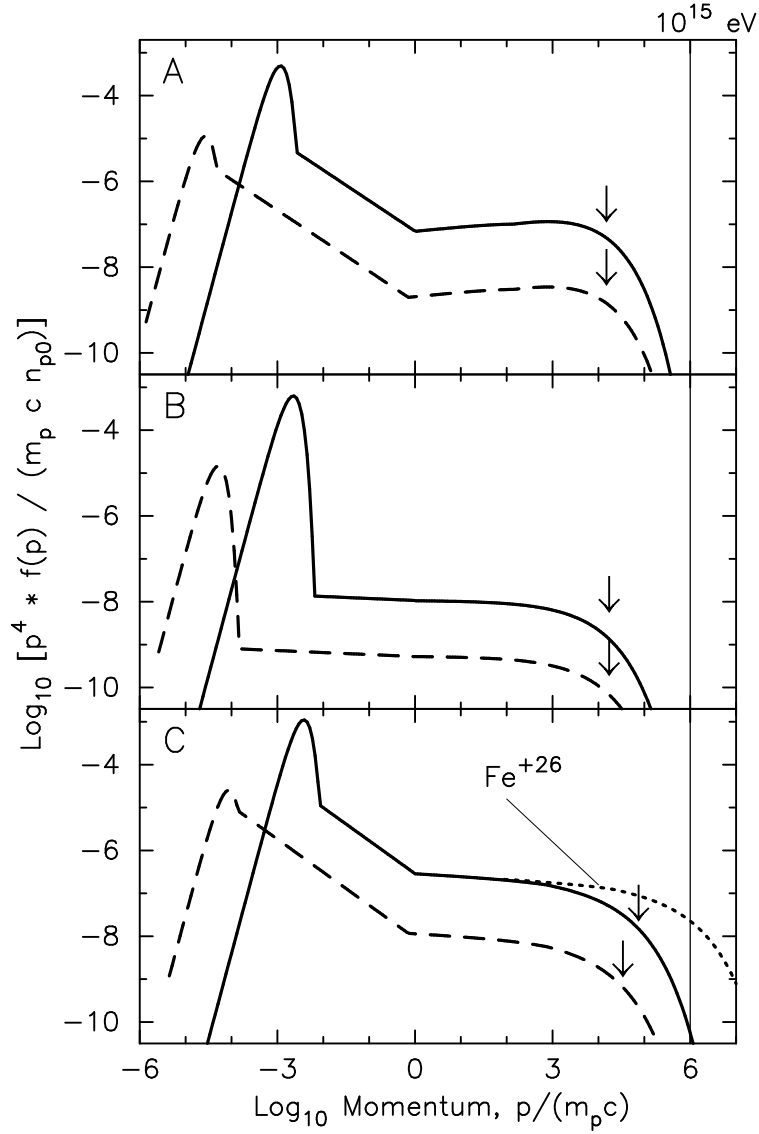


Fig. 5.— Proton (solid curves) and electron spectra (dashed curves) for models *A*, *B*, and *C* used to generate the photon spectra shown in Figure 3. The arrows indicate $E_{\text{max,p}}$ and $E_{\text{max,e}}$. The dotted curve in the bottom panel shows the high momentum portion of a possible Fe^{+26} spectrum from Model *C*. The normalization relative to protons is that shown in Figure 8 of Ellison, Drury, & Meyer (1997).

interacts with the interstellar medium (or with a slower red supergiant wind). This suggests the shock is still within the low density bubble but has encountered a density enhancement perhaps caused by perturbations in the pre-SN wind.

We put limits on the acceleration efficiency and find that G347.3–0.5 is currently putting at least 25% (and more likely $\sim 50\%$) of the forward shock ram energy flux into relativistic particles (i.e., cosmic rays). Recently, Hughes, Rakowski, & Decourchelle (2000) have inferred efficient shock acceleration in SNR E0102.2-7219 in the Small Magellanic Cloud from the shock speed, determined from expansion measurements, and the postshock electron temperature, determined from X-ray line models (unlike G347.3–0.5, lines are visible above the synchrotron continuum in the post-forward shock gas). They concluded that the extremely low postshock temperature can only be reconciled with the high shock speed if a sizable fraction ($\sim 50\%$) of the shock energy goes into cosmic rays. Our results are fully consistent with this and with the important point that efficient particle acceleration causes a strong coupling between the broad-band emission from relativistic particles and the properties of the shocked heated X-ray emitting gas (see Decourchelle, Ellison, & Ballet 2000). We have verified that Sedov models (not shown) with no density enhancement produce satisfactory nonlinear fits to the observed spectral shape with input parameters similar to those given here, but are inconsistent with the observed remnant diameter and distance.¹³ We conclude that the nonlinear aspects we infer, in particular the required high acceleration efficiency, do not depend significantly on the geometric details of the wind-shell model while the overall normalization does.

Furthermore, we find that the maximum energies of the cosmic-ray electrons and protons are well below 10^{15} eV. While it has been known for some time that SNRs emitting nonthermal X-rays do not produce *electrons* to energies near 10^{15} eV (e.g., Reynolds & Keohane 1999), the nonlinear effects we model make it possible to infer the proton distribution from photons emitted by electrons. For no magnetic field compression in the shock and other parameters adjusted to produce the highest possible $E_{\text{max,p}}$ and still give a reasonable fit to the observations, we find a proton maximum energy $\lesssim 70$ TeV. More realistic parameters with magnetic field compression yield $E_{\text{max,p}} \sim 20$ TeV. However, SNR shocks will also accelerate heavier ion species such as He, C, O, and Fe, and the maximum energy in diffusive shock acceleration scales as charge. Therefore, this SNR could produce a power-law Fe^{+26} spectrum to $\sim 10^{15}$ eV. To illustrate, we have estimated the Fe^{+26} spectrum produced by our model *C* and placed it in the bottom panel of Figure 5. The normalization is determined by the cosmic abundance of iron ($\sim 3.1 \times 10^{-5}$ iron nuclei for every proton) plus the enhancement expected because iron is injected and initially accelerated when it is trapped in dust grains. In fact, the normalization of iron relative to hydrogen in Figure 5 is

¹³In standard Sedov models, the relatively high shock speeds and ambient densities which produce acceptable fits to the observed shape occur at shock radii which are too small to be consistent with a remnant diameter of $45'$ (or even $30'$) at $D_{\text{snr}} \sim 6$ kpc. Only if $D_{\text{snr}} < 3$ kpc could standard models produce acceptable fits. The wind-shell model allows the shock to propagate for large distances in the low density wind before encountering the higher density emission region.

just that shown in Figure 8 of Ellison, Drury, & Meyer (1997) at 10^8 keV/nucleon. Cosmic-ray observations in the $10^{14} - 10^{16}$ eV range typically measure the total energy of the particles and have large uncertainties in differentiating individual ion species (e.g., Bernlöhner et al. 1998; Glasmacher et al. 1999; Swordy & Kieda 2000). Nevertheless, a number of authors have produced models of this transition energy range adding together the fluxes from different ion species with cutoffs that scale as charge (e.g., Stanev, Biermann, & Gaisser 1993; Erlykin & Wolfendale 2000). Our high B_0 results are in general agreement with this work.

The authors thank J. Blondin and the referee A. Decourchelle for helpful comments. This work was supported in part by the National Aeronautics and Space Administration through contract NAS8-39073 and grant NAG5-4803. The Australia Telescope is funded by the Commonwealth of Australia for operation as a National Facility managed by CSIRO. B.M.G. acknowledges the support of NASA through Hubble Fellowship grant HF-01107.01-98A awarded by the Space Telescope Science Institute, which is operated by the Association of Universities for Research in Astronomy, Inc., for NASA under contract NAS 5-26555.

REFERENCES

- Achterberg, A., Blandford, R. D., & Reynolds, S. P. 1994, *A&A*, 281, 220
- Allen, G. E. et al. 1997, *ApJ*, 487, L97
- Axford, W. I. 1981, *Proc. 17th Int. Cosmic Ray Conf. (Paris)*, 12, 155
- Baring, M. G., Ogilvie, K. W., Ellison, D. C., & Forsyth, R. J. 1997, *ApJ*, 476, 889
- Baring, M. G., Ellison, D. C., Reynolds, S. P., Grenier, I. A. & Goret, P., 1999, *ApJ*, 513, 311
- Berezhko, E. G., & Ellison, D. C. 1999, *ApJ*, 526, 385
- Berezhko, E. G., Ksenofontov, L. T., & Petukhov, S. I., 1999, *Proc. 26th Int. Cosmic Ray Conf. (Salt Lake City)*, 99, 4431
- Berezhko, E. G., & Völk, H. J. 1997, *Astroparticle Phys.*, 7, 183
- Berezhko, E. G., & Völk, H. J. 2000, *A&A*, 357, 283
- Bernlöhner, K., Hofmann, W., Leffers, G., Matheis, V., Panter, M., & Zink, R. 1998, *Astroparticle Phys.*, 8, 253
- Blandford, R. D., & Eichler, D. 1987, *Physics Reports*, 154, 1
- Blondin, J. M., & Ellison, D. C. 2001, *ApJ*, in press [[astro-ph/0104024](#)]
- Chevalier, R. A. 1982a, *ApJ*, 258, 790

- Chevalier, R. A. 1982b, *ApJ*, 259, L85
- Decourchelle, A., Ellison, D. C., & Ballet, J., 2000, *ApJ*, 543, L57
- Drury, L. O’C. 1983, *Rep. Prog. Phys.*, 46, 973
- Drury, L. O’C., Markiewicz, W. J., & Völk, H. J. 1989, *A&A*, 225, 179
- Dwarkadas, V. V., & Chevalier, R. A. 1998, *ApJ*, 497, 807
- Eichler, D. 1981, *ApJ*, 247, 1089
- Ellison, D. C. 1985, *J.G.R.*, 90, 29
- Ellison, D. C., Baring, M. G., & Jones, F. C. 1996, *ApJ*, 473, 1029
- Ellison, D. C., Berezhko, E. G., & Baring, M. G. 2000, *ApJ*, 540, 292
- Ellison, D. C., Jones, F. C., & Baring, M. G. 1999, *ApJ*, 512, 403
- Ellison, D. C., Drury, L. O’C., & Meyer, J.-P. 1997, *ApJ*, 487, 197
- Ellison, D.C., Möbius, E., & Paschmann, G., 1990, *ApJ*, 352, 376
- Erlykin, A. D., & Wolfendale, A. W. 2000, *A&A*, 356, L63
- Glasmacher, M.A.K., et al. 1999, *Astroparticle Phys.*, 10, 291
- Gehrels, N. & Michelson, P. 1999, *Astroparticle Phys.*, 11, 277.
- Gull, S. F. 1975, *M.N.R.A.S.*, 171, 263
- Hughes, J. P., Rakowski, C. E., & Decourchelle, A. 2000, *ApJ*, 543, L61
- Jones, F.C., & Ellison, D.C. 1991, *Space Sci. Rev.*, 58, 259
- Jun, B.-I., & Jones, T. W. 1999, *ApJ*, 511, 774
- Kang, H. & Jones, T. W. 1997, *ApJ*, 476, 875
- Kazanas, D., & Ellison, D. C. 1986, *ApJ*, 304, 178
- Keohane, J. W., Gotthelf, E. V., & Petre, R. 1998, *ApJ*, 503, L175
- Koyama, K., Petre, R., Gotthelf, E. V., Hwang, U., Matsuura, M., Ozaki, M., & Holt, S. S. 1995, *Nature*, 378, 255
- Lucek, S. G., & Bell, A. R. 2000, *M.N.R.A.S.*, 314, 65
- Malkov, M. 1997, *ApJ*, 485, 638

- Mastichiadis, A. & de Jager, O. C. 1996, *A&A*, 311, L5
- Meyer, J.-P., Drury, L. O’C., & Ellison, D. C. 1997, *ApJ*, 487, 182
- Muraishi, H., et al. 2000, *A&A*, 354, L57
- Pfeffermann, E., & Aschenbach, B. 1996, in *Roentgenstrahlungen from the Universe*, ed. H. H. Zimmermann, J. Trümper, & H. Yorke (MPE Rep. 263; Garching: MPE), 267
- Raymond, J. C., & Smith, G. W. 1977, *ApJS*, 35, 49
- Reynolds, S. P. 1998, *ApJ*, 493, 375
- Reynolds, S. P. & Keohane, J.W., 1999, *ApJ*, 525, 368
- Sault, R. J., Staveley-Smith, L., & Brouw, W. N. 1996, *A&AS*, 120, 375
- Scholer, M., Trattner, K.J., & Kucharek, H. 1992, *ApJ*, 395, 675
- Slane, P., Gaensler, B. M., Dame, T. M., Hughes, J. P., Plucinsky, P. P., & Green, A. 1999, *ApJ*, 525, 357
- Stanev, T., Biermann, P. L., & Gaisser, T. K. 1993, *A&A*, 274, 902
- Swordy, S. P., & Kieda, D. B. 2000, *Astroparticle Phys.*, 13, 137
- Tanimori, T., et al. 1998, *ApJ*, 497, L25
- Terasawa, T., et al. 1999, *Proc. 26th Int. Cosmic Ray Conf. (Salt Lake City)*, 6, 528
- Völk, H. J. 2001, to appear in the Proceedings of the XXIst Rencontres de Moriond “Very High Energy Phenomena in the Universe,” Les Arcs, France, Jan. 20-27, 2001 [astro-ph/0105356]
- Weekes, T. C., et al. 1999, VERITAS proposal [<http://egret.sao.arizona.edu/vhegra/vhegra.html>]
- Winkler, C. 1996, *A&AS*, 120, 637 see also [<http://astro.estec.esa.nl/SA-general/Projects/Integral/>]